

AD-A135 711

SOLUTION PROCEDURES FOR ACCURATE NUMERICAL SIMULATIONS  
OF FLOW IN TURBOMACHINERY (U) MASSACHUSETTS INST OF TECH  
CAMBRIDGE DEPT OF AERONAUTICS AND A.S.

1/1

UNCLASSIFIED

W T THOMPkins ET AL. JAN 83

F/G 20/4

NL

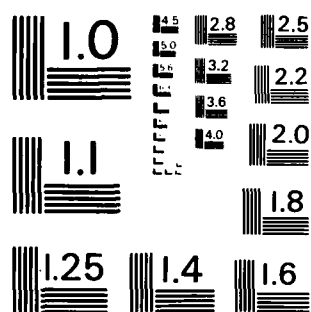
END

DATE

FILED

1-84

DTIC



MICROCOPY RESOLUTION TEST CHART  
NATIONAL BUREAU OF STANDARDS-1963-A

# AIAA'83

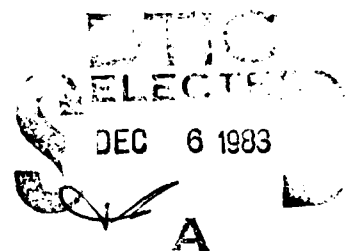
AFOSR-TR-83-1022

**AD-A136-711**

**AIAA-83-0257**

## **Solution Procedures for Accurate Numerical Simulations of Flow in Turbomachinery Cascades**

W.T. Thompkins, Jr., S.S. Tong, R.H.  
Bush, W.J. Usab, Jr. and R.J.G. Norton,  
Massachusetts Institute of Technology,  
Cambridge, MA



DTIC FILE COPY

## **AIAA 21st Aerospace Sciences Meeting**

January 10-13, 1983/Reno, Nevada

Approved for public release  
Distribution unlimited.

For permission to copy or republish, contact the American Institute of Aeronautics and Astronautics  
1290 Avenue of the Americas, New York, NY 10104

83 12 135

UNCLASSIFIED

SECURITY CLASSIFICATION OF THIS PAGE (When Data Entered)

| REPORT DOCUMENTATION PAGE   |   | READ INSTRUCTIONS<br>BEFORE COMPLETING FORM   |
|---|---|---|
| 1. REPORT NUMBER<br><b>AFOSR-TR. 83-1022</b>  | 2. GOVT ACCESSION NO.<br><b>A135711</b> | 3. RECIPIENT'S CATALOG NUMBER   |
| 4. TITLE (and Subtitle)<br><b>SOLUTION PROCEDURES FOR ACCURATE NUMERICAL<br/>SIMULATIONS OF FLOW IN TURBOMACHINERY CASCADES</b>   |   | 5. TYPE OF REPORT & PERIOD COVERED<br><b>INTERIM</b>  |
|   |   | 6. PERFORMING ORG. REPORT NUMBER  |
| 7. AUTHOR(s)<br><b>W T THOMPkins JR                      W J USAB JR<br/>S S TONG                                  R J G NORTON<br/>R H BUSH</b>  |   | 8. CONTRACT OR GRANT NUMBER(s)<br><b>F49620-82-K-0002</b>                                   |
| 9. PERFORMING ORGANIZATION NAME AND ADDRESS<br><b>MASSACHUSETTS INSTITUTE OF TECHNOLOGY<br/>DEPT OF AERONAUTICS &amp; ASTRONAUTICS<br/>CAMBRIDGE, MA 02139</b>  |   | 10. PROGRAM ELEMENT, PROJECT, TASK<br>AREA & WORK UNIT NUMBERS<br><b>61102F<br/>2307/A4</b> |
| 11. CONTROLLING OFFICE NAME AND ADDRESS<br><b>AIR FORCE OFFICE OF SCIENTIFIC RESEARCH/NA<br/>BOLLING AFB, DC 20332</b>  |   | 12. REPORT DATE<br><b>January 1983</b>  |
|   |   | 13. NUMBER OF PAGES<br><b>16</b>  |
| 14. MONITORING AGENCY NAME & ADDRESS (if different from Controlling Office)   |   | 15. SECURITY CLASS. (of this report)<br><b>Unclassified</b>                                 |
|   |   | 15a. DECLASSIFICATION DOWNGRADING<br>SCHEDULE   |
| 16. DISTRIBUTION STATEMENT (of this Report)<br><br><b>Approved for Public Release; Distribution Unlimited.</b>  |   |   |
| 17. DISTRIBUTION STATEMENT (of the abstract entered in Block 20, if different from Report)  |   |   |
| 18. SUPPLEMENTARY NOTES<br><br><b>Proceedings of the AIAA Aerospace Sciences Meeting, 21st Reno, Nevada<br/>10-13 January 1983, The American Institute of Aeronautics &amp; Astronautics 1983</b>   |   |   |
| 19. KEY WORDS (Continue on reverse side if necessary and identify by block number)<br><b>NUMERICAL METHODS<br/>FINITE DIFFERENCE<br/>FINITE VOLUME<br/>CASCADES<br/>NUMERICAL ACCURACY</b>  |   |   |
| 20. ABSTRACT (Continue on reverse side if necessary and identify by block number)<br><b>For several years the authors have been involved in evaluating and developing<br/>numerical simulation schemes for compressible, two dimensional inviscid or<br/>viscous flows in turbomachinery cascades. Numerical schemes considered<br/>were all originally classified as time-marching schemes and include: 1)<br/>implicit approximate factorization schemes like those of Beam and Warming,<br/>2) explicit schemes due to McCormack, 3) explicit central difference schemes<br/>due to Jameson, Schmidt and Turkel and Rizzi, and 4) the multi-grid scheme<br/>of Ni. As we have developed these schemes we have come to believe that</b> |   |   |

DD FORM 1 JAN 73 1473 EDITION OF 1 NOV 65 IS OBSOLETE

UNCLASSIFIED

SECURITY CLASSIFICATION OF THIS PAGE (When Data Entered)

UNCLASSIFIED

SECURITY CLASSIFICATION OF THIS PAGE (When Data Entered)

the accuracy of computational results is relatively insensitive to the numerical algorithm chosen but highly sensitive to implementation details such as boundary conditions, consistent flux balancing, grid resolution and numerical smoothing. In order to illustrate our viewpoint, we present an examination of the relationship between a flux balancing interpretation of the control volume conservation laws and various finite difference formulations and comparisons of the performance of these schemes on three test problems: Ni's bump in a channel, a supersonic nozzle, and flow in a supercritical compressor cascade. As final test example, a comparison is made between measured and computed flow, using a compressible, Navier-Stokes solver, for a high speed turbine cascade.

UNCLASSIFIED

SECURITY CLASSIFICATION OF THIS PAGE (When Data Entered)

# SOLUTION PROCEDURES FOR ACCURATE NUMERICAL SIMULATIONS OF FLOW IN TURBOMACHINERY CASCADES

W. T. THOMPkins Jr.\*  
S. S. TONG\*\*  
R. H. BUSH\*\*  
W. J. USAB Jr.\*\*  
R. J. G. NORTON\*\*\*

Massachusetts Institute of Technology  
Cambridge, Massachusetts



A-1  
10/1/73  
10/1/73  
10/1/73

## Abstract

For several years the authors have been involved in evaluating and developing numerical simulation schemes for compressible, two dimensional inviscid or viscous flows in turbomachinery cascades. Numerical schemes considered were all originally classified as time-marching schemes and include: 1) implicit approximate factorization schemes like those of Beam and Warming, 2) explicit schemes due to MacCormack, 3) explicit central difference schemes due to Jameson, Schmidt and Turkel and Rizzi, and 4) the multi-grid scheme of Ni. As we have developed these schemes we have come to believe that the accuracy of computational results is relatively insensitive to the numerical algorithm chosen but highly sensitive to implementation details such as boundary conditions, consistent flux balancing, grid resolution and numerical smoothing. In order to illustrate our viewpoint, we present an examination of the relationship between a flux balancing interpretation of the control volume conservation laws and various finite difference formulations and comparisons of the performance of these schemes on three test problems: Ni's bump in a channel, a supersonic nozzle, and flow in a supercritical compressor cascade. As a final test example, a comparison is made between measured and computed flow, using a compressible, Navier-Stokes solver, for a high speed turbine cascade.

## Finite Difference Operator Definitions

$$\delta_j^0 u_{j,k} = \frac{1}{2}(u_{j+1,k} - u_{j-1,k})$$

$$u_j^+ u_{j,k} = \frac{1}{2}(u_{j+1,k} + u_{j,k})$$

$$u_j^- u_{j,k} = \frac{1}{2}(u_{j,k} + u_{j-1,k})$$

$$\delta_j^+ u_{j,k} = u_{j+1,k} - u_{j,k}$$

$$\delta_j^- u_{j,k} = u_{j,k} - u_{j-1,k}$$

$$\delta_{j/2}^0 u_{j,k} = u_{j+\frac{1}{2},k} - u_{j-\frac{1}{2},k}$$

Note that all coordinate positions at non-integer mesh spacing are to be defined by simple averages,

$$y_{j+\frac{1}{2},k} = \frac{1}{2}(y_{j,k} + y_{j+1,k})$$

\*Associate Professor, Department of Aeronautics and Astronautics; Member AIAA

\*\*Research Assistant, Department of Aeronautics and Astronautics

\*\*\*Visiting Engineer; permanent affiliation: Rolls-Royce, Inc., Atlanta, Georgia

Copyright © American Institute of Aeronautics and Astronautics, Inc., 1983. All rights reserved.

## INTRODUCTION

For several years the authors have been involved in evaluating and developing numerical methods for compressible, inviscid or viscous, internal flow problems. The methods discussed in this paper include (1) implicit approximation factorization schemes due to Beam and Warming [1], (2) explicit schemes due to MacCormack [2], (3) an explicit central difference scheme suggested by Jameson, Schmidt and Turkel [3] and Rizzi [4], and (4) the multi-grid scheme due to Ni [5]. Most of these methods were originally formulated as time-marching methods although all are now run as pseudo-time-marching methods.

Throughout these evaluations we have been interested primarily in the accuracy of the steady state solutions rather than the computer run time or number of iterations to convergence. As we have developed these methods we have come to believe that the accuracy of the computational results is relatively insensitive to the numerical scheme chosen, but it is highly sensitive to implementation details such as boundary conditions, consistent flux balancing, grid resolution and numerical smoothing.

In order to illustrate our viewpoint we first present an examination of the relationship between a flux balancing or finite volume interpretation of the control volume conservation laws and a finite difference formulation in strong conservation law form. While the development here is perhaps not unique or entirely new, it is essential for understanding the relationships between various numerical schemes. Next we present a development, from a flux balance viewpoint, of the several schemes which emphasizes their basic similarity rather than their computational differences. The conclusion here is that all these schemes should produce nearly the same steady state solutions when the same boundary conditions and smoothing operators are applied. Results from three inviscid computational test problems are then presented in order to demonstrate the validity of this conclusion. Lastly, results from computations using a full Navier-Stokes version of the Beam-Warming algorithm are compared to experimental results for a high speed, high turning turbine cascade. These results illustrate that a consistent application of the flux balancing analysis can produce accurate solutions even in extreme geometries with rather modest cost. The number of iterations to full convergence is about 500 for a grid containing 100x50 nodes.

AIR FORCE OFFICE OF SCIENTIFIC RESEARCH (AFOSR)  
NOTICE OF AWARD  
This award is made under the terms of the AFOSR-12-100-12.

1 MATTHEW J. ...  
Chief, Technical Information Division

# ANALYSIS

## Relationship Between Finite Difference and Finite Volume Interpretations

Consider the two-dimensional Euler equation expressed in conservation law form:

$$\frac{\partial U}{\partial t} + \frac{\partial F}{\partial x} + \frac{\partial G}{\partial y} = 0, \quad (1)$$

$$U = \begin{pmatrix} \rho \\ \rho u \\ \rho v \\ \rho E \end{pmatrix} \quad F = \begin{pmatrix} \rho u \\ \rho u^2 + P \\ \rho uv \\ \rho u(E+P/\rho) \end{pmatrix} \quad G = \begin{pmatrix} \rho v \\ \rho uv \\ \rho v^2 + P \\ \rho v(E+P/\rho) \end{pmatrix},$$

and a coordinate system transformation,

$$\xi = \xi(x, y) \quad \eta = \eta(x, y) \quad t = t. \quad (2)$$

The strong conservation law form under this transformation is retained as, reference [6]:

$$\frac{\partial(U/J)}{\partial t} + \frac{\partial(F/J \frac{\partial \xi}{\partial x} + G/J \frac{\partial \xi}{\partial y})}{\partial \xi} + \frac{\partial(F/J \frac{\partial \eta}{\partial x} + G/J \frac{\partial \eta}{\partial y})}{\partial \eta} = 0, \quad (3)$$

where  $J$  is the transformation Jacobian

$$\left( \frac{\partial \xi}{\partial x} \right) \left( \frac{\partial \eta}{\partial y} \right) - \left( \frac{\partial \xi}{\partial y} \right) \left( \frac{\partial \eta}{\partial x} \right). \quad (4)$$

In shorthand notation, equation (3) becomes:

$$\hat{U}_t + \hat{F}_\xi + \hat{G}_\eta = 0, \quad (5)$$

where

$$\hat{U} = \frac{U}{J},$$

$$\hat{F} = \frac{F}{J} \xi_x + \frac{G}{J} \xi_y,$$

$$\hat{G} = \frac{F}{J} \eta_x + \frac{G}{J} \eta_y,$$

$$J = \xi_x \eta_y - \xi_y \eta_x.$$

Formal relationships exist between the transformation from  $(x, y)$  coordinates to  $(\xi, \eta)$  coordinates and the inverse transformation from  $(\xi, \eta)$  coordinates to  $(x, y)$  coordinates which are:

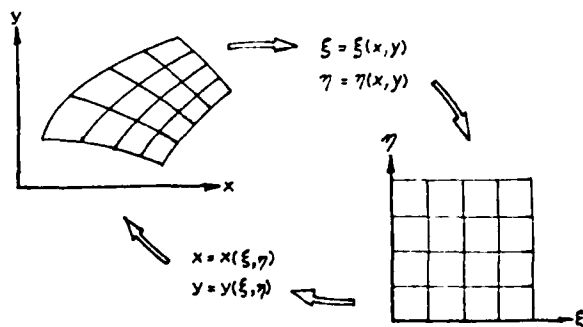


Figure 1. Relationship between transformation from physical to computational space and computational to physical space.

$$\begin{aligned} x_{,\xi} &= \eta_{,y}/J, & y_{,\xi} &= -\eta_{,x}/J, \\ x_{,\eta} &= -\xi_{,y}/J, & y_{,\eta} &= \xi_{,x}/J, \end{aligned} \quad (6)$$

and the inverse Jacobian is

$$J^{-1} = x_{,\xi} y_{,\eta} - x_{,\eta} y_{,\xi} = 1/J.$$

The Jacobians express the ratio of cell areas between the different representations.

The transformation metrics  $(\xi_x, \xi_y, \eta_x, \eta_y)$  are most conveniently obtained, as suggested by Steger [7], from a finite difference evaluation of these derivatives in computational space using equations (6). This process uses only the fact that the coordinate transformation is a one-to-one mapping. If we consider all these derivatives to be evaluated by centered finite differences, we have, assuming  $\Delta \xi = \Delta \eta = 1$ ,

$$\left( \frac{\xi_x}{J} \right)_{j,k} = \delta_k^0 y_{j,k} = \frac{(y_{j,k+1} - y_{j,k-1}))}{2} \quad (7)$$

$$\left( \frac{\xi_y}{J} \right)_{j,k} = -\delta_k^0 x_{j,k} = \frac{-(x_{j,k+1} - x_{j,k-1}))}{2} \quad (8)$$

$$\left( \frac{\eta_x}{J} \right)_{j,k} = -\delta_j^0 y_{j,k} = \frac{-(y_{j+1,k} - y_{j-1,k}))}{2} \quad (9)$$

$$\left( \frac{\eta_y}{J} \right)_{j,k} = \delta_j^0 x_{j,k} = \frac{(x_{j+1,k} - x_{j-1,k}))}{2} \quad (10)$$

If we consider the computational cells to be polygons, the exact area of a cell can be determined, see [8], from

$$\text{Area} = \frac{1}{2} \left\{ \sum_{i=1}^N x_i y_{i+1} - \sum_{i=1}^N x_{i+1} y_i \right\} \quad (11)$$

where  $N$  is the number of edge nodes, and

$$i+1 = \begin{cases} i+1 & \text{if } i+1 \leq N \\ 1 & \text{if } i+1 > N \end{cases}.$$

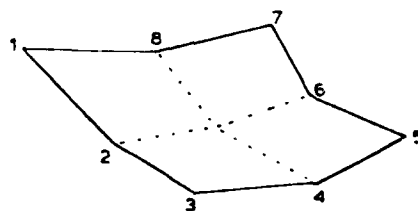


Figure 2. Node connection diagram for general computational cell polygon.

Now consider a possible finite difference representation of equation (5),

$$\left(\frac{\partial U/J}{\partial t}\right)_{j,k}^n = -\delta_j^0 \hat{F}_{j,k} - \delta_k^0 \hat{G}_{j,k}, \quad (12)$$

on a standard 9 point cell,

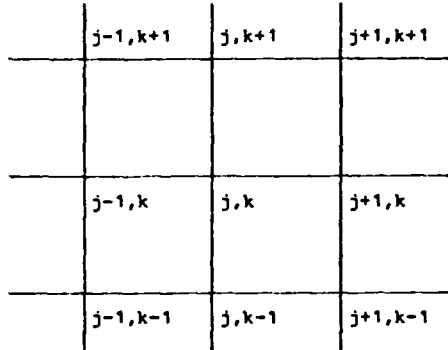


Figure 3. Finite difference node numbering scheme.

$$\begin{aligned} \left(\frac{\partial (U/J)}{\partial t}\right)_{j,k}^n = & \frac{1}{2} \left\{ \left(F \frac{\xi_x}{J}\right)_{j+1,k} + \left(G \frac{\xi_y}{J}\right)_{j+1,k} \right. \\ & - \left(F \frac{\xi_x}{J}\right)_{j-1,k} - \left(G \frac{\xi_y}{J}\right)_{j-1,k} \\ & + \left(F \frac{\eta_x}{J}\right)_{j,k+1} + \left(G \frac{\eta_y}{J}\right)_{j,k+1} \\ & \left. - \left(F \frac{\eta_x}{J}\right)_{j,k-1} - \left(G \frac{\eta_y}{J}\right)_{j,k-1} \right\} \quad (13) \end{aligned}$$

Now replacing the metric derivatives with their finite difference expressions, equations (7) through (11), and writing out only the continuity equation for clarity, we have

$$\begin{aligned} \left(\frac{\partial \rho/J}{\partial t}\right)_{j,k}^n = & -\frac{1}{4} \left\{ \left[ (\rho u)_{j+1,k}^n (y_{j+1,k+1} - y_{j+1,k-1}) \right. \right. \\ & - (\rho v)_{j+1,k}^n (x_{j+1,k+1} - x_{j+1,k-1}) \\ & - \left[ (\rho u)_{j-1,k}^n (y_{j-1,k+1} - y_{j-1,k-1}) \right. \\ & - (\rho v)_{j-1,k}^n (x_{j-1,k+1} - x_{j-1,k-1}) \\ & + \left[ -(\rho u)_{j,k+1}^n (y_{j+1,k+1} - y_{j-1,k+1}) \right. \\ & \left. \left. + (\rho v)_{j,k+1}^n (x_{j+1,k+1} - x_{j-1,k+1}) \right] \right\} \end{aligned}$$

$$\begin{aligned} & - \left[ -(\rho u)_{j,k-1}^n (y_{j+1,k-1} - y_{j-1,k-1}) \right. \\ & \left. + (\rho v)_{j,k-1}^n (x_{j+1,k-1} - x_{j-1,k-1}) \right] \} \quad (14) \end{aligned}$$

or

$$\begin{aligned} \left(\frac{\partial (U/J)}{\partial t}\right)_{j,k}^n = & -\left(\delta_j^0 F C_{j,k}^n + \delta_k^0 G C_{j,k}^n\right) \\ = & - (RC)_{j,k}^n. \quad (15) \end{aligned}$$

This form of the continuity equation is identical to that which would be obtained by an integration of the control volume fluid equations around the cell area, assuming no variation of  $(\rho u)$  or  $(\rho v)$  across a cell face.

Again using only the continuity equation for clarity,

$$\frac{\partial}{\partial t} \int_{\text{area}} \rho dx dy = - \int_{\text{control surface}} \rho (u \hat{i}_x + v \hat{i}_y) \cdot \bar{n} dl \quad (16)$$

where  $\hat{i}_x, \hat{i}_y$  are unit vectors in original Cartesian coordinates,

$\bar{n}$  is an outward normal vector to the cell face, and

$dl$  is length along the face.

Equation (16), when expanded, is identical to equation (14), and shows that the proper interpretation of a metric derivative is that the ratio of that derivative to the Jacobian is the projected area of the face. Thus the solution of a finite difference problem in strong conservation law form in a transformed space is equivalent to the solution of a flux summation algorithm expressed in physical space.

The flux sum of equation (13) could be improved by selecting a more accurate approximation for the integral of  $(\rho u)$  or  $(\rho v)$  over a face than simply its value at the center of the face. For example, a piecewise continuous interpretation of  $(\rho u)$  is equivalent to

$$\begin{aligned} \int (\rho u \hat{i}_x) \cdot \bar{n} dl = & \left( u_k^+ (\rho u)_{j,k} \right) \delta_k^+ y_{j,k} \\ & + \left( u_k^- (\rho u)_{j,k} \right) \delta_k^- y_{j,k}. \quad (17) \end{aligned}$$

An important property of equation (14) is that a uniform solution  $\{(\rho u)_{j,k}, (\rho v)_{j,k}\}$  constant over space remains identically uniform. This property is generally referred to as area conservation in finite element analysis and its importance to maintaining constant freestream solutions was first pointed out by Steger [7]. A recent paper by Hindman [9] has also emphasized this property.



COMPARISON OF FLUX BALANCE FORM OF SEVERAL  
TIME-MARCHING ALGORITHMS FOR INVISCID FLOW

Centered Difference Algorithms

METHOD A. Implicit Time-Marching Algorithm of  
Beam and Warming [1]:

The first method to be considered is the time marching algorithm introduced by Beam and Warming which is unconditionally stable, in the linear problem, for two dimensional flows:

$$\begin{aligned} (I + \Delta t L_{\xi}^I) (I + \Delta t L_{\eta}^I) (\hat{U}_{j,k}^{n+1} - \hat{U}_{j,k}^n) = \\ = - \Delta t (\delta_j^0 FC_{j,k}^n + \delta_k^0 GC_{j,k}^n - L_{BWAV} \hat{U}_{j,k}^n) \\ = - \Delta t (RC_{j,k}^n - L_{BWAV} \hat{U}_{j,k}^n), \end{aligned} \quad (18)$$

where  $L_{\xi}^I$  and  $L_{\eta}^I$  are finite difference operators whose form determines the order of accuracy of the time-marching algorithm and  $L_{BWAV}$  is a finite difference smoothing operator.

Solution Procedure

Step 1:

$$(I + \Delta t L_{\xi}^I) (\hat{U}_{j,k}^{n+1}) = - \Delta t (RC_{j,k}^n - L_{BWAV} \hat{U}_{j,k}^n) \quad (19)$$

Step 2:

$$(I + \Delta t L_{\eta}^I) \hat{U}_{j,k}^{n+1} = \hat{U}_{j,k}^{n+1} \quad (20)$$

Step 3:

$$\hat{U}_{j,k}^{n+1} = \hat{U}_{j,k}^n + \Delta \hat{U}_{j,k}^{n+1} \quad (21)$$

METHOD B. Modified Beam and Warming Algorithm

In order to improve the accuracy of the flux balance operator in skewed mesh systems, a variety of modified Beam and Warming algorithms have been developed. The simplest modified operator, which corresponds to several other algorithms, is to balance the flux on the cell shown below.

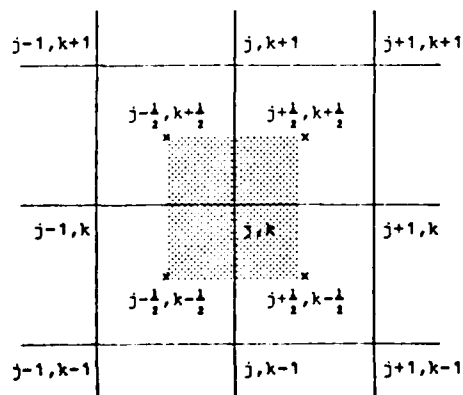


Figure 4. Half-spacing mesh cell in computational space.

The flux balance operator is:

$$RCH_{j,k}^n = \delta_{j/2}^0 (FCH)_{j,k}^n + \delta_{k/2}^0 (GCH)_{j,k}^n, \quad (22)$$

where

$$\begin{aligned} (FCH)_{j \pm \frac{1}{2}, k}^n &= \left( u_j^{\pm} F_{j,k}^n \right) \left( u_j^{\pm} \delta_{k/2}^0 y_{j,k} \right) \\ &\quad - \left( u_j^{\pm} G_{j,k}^n \right) \left( u_j^{\pm} \delta_{k/2}^0 x_{j,k} \right) \\ (GCH)_{j, k \pm \frac{1}{2}}^n &= - \left( u_k^{\pm} F_{j,k}^n \right) \left( u_k^{\pm} \delta_{j/2}^0 y_{j,k} \right) \\ &\quad + \left( u_k^{\pm} G_{j,k}^n \right) \left( u_k^{\pm} \delta_{j/2}^0 x_{j,k} \right), \end{aligned}$$

and the algorithm becomes

$$\begin{aligned} (I + \Delta t_{j,k} L_{\xi}^I) (I + \Delta t_{j,k} L_{\eta}^I) (\hat{U}_{j,k}^{n+1} - \hat{U}_{j,k}^n) \\ = - \Delta t_{j,k} (RCH)_{j,k}^n - L_{BWAV} \hat{U}_{j,k}^n. \end{aligned} \quad (23)$$

METHOD C. Explicit Time Integration Scheme of  
Jameson [3] and Rizzi [4]:

The Runge-Kutta time stepping approach can be expressed as:

$$\frac{d\hat{U}_{j,k}}{dt} = - RCH_{j,k}^n + L_{RKAV} \hat{U}_{j,k}^n = - P\hat{U}_{j,k}^n \quad (24)$$

Step 1:

$$\hat{U}^{(0)} = \hat{U}_{j,k} \quad (25)$$

Step 2:

$$\hat{U}^{(1)} = \hat{U}^{(0)} - \left( \frac{\Delta t}{2} \right)_{j,k} P\hat{U}^{(0)} \quad (26)$$

Step 3:

$$\hat{U}^{(2)} = \hat{U}^{(0)} - \left( \frac{\Delta t}{2} \right)_{j,k} P\hat{U}^{(1)} \quad (27)$$

Step 4:

$$\hat{U}^{(3)} = \hat{U}^{(0)} - \Delta t_{j,k} P\hat{U}^{(2)} \quad (28)$$

Step 5:

$$\begin{aligned} \hat{U}^{(4)} &= \hat{U}^{(0)} \\ &\quad - \left( \frac{\Delta t}{6} \right)_{j,k} \left( P\hat{U}^{(0)} + 2P\hat{U}^{(1)} + 2P\hat{U}^{(2)} + P\hat{U}^{(3)} \right) \end{aligned} \quad (29)$$

Step 6

$$\hat{U}_{j,k}^{n+1} = \hat{U}^{(4)} \quad (30)$$

This method is usually run with the smoothing operator in each step formed as  $L_{RKAV} \hat{U}^n$  rather than  $L_{RKAV} \hat{U}^{(1)}$ .

If steps 2, 3, 4, 5 each converge independently, then the steady state solution is identical to that of the modified Beam and Warming, method B, if  $L_{BWAV} = L_{RKAV}$ , and the solution is independent of  $\Delta t_{j,k}$ .

#### METHOD D. Flux Balance Form of MacCormack's Method [2]:

A flux balance form of MacCormack's method may be expressed as:

##### Step 1, Predictor:

$$\begin{aligned} \hat{U}_{j,k}^{*1} = & \hat{U}_{j,k}^n - \Delta t_{j,k} \left[ (F_{j+1,k}^{n,PLy1} - G_{j+1,k}^{n,PLx1}) \right. \\ & - (F_{j,k}^{n,PLy3} - G_{j,k}^{n,PLx3}) \\ & + (-F_{j,k+1}^{n,PLy4} + G_{j,k+1}^{n,PLx4}) \\ & - (-F_{j,k}^{n,PLy2} + G_{j,k}^{n,PLx2}) \\ & \left. - L_{MAV} \hat{U}_{j,k}^n \right] \end{aligned} \quad (31)$$

where the projected lengths are

$$PL_{y1} = v_j^+ \delta_{k/2}^0 y_{j,k} = y_{j+\frac{1}{2},k+\frac{1}{2}} - y_{j+\frac{1}{2},k-\frac{1}{2}}$$

⋮

$$PL_{x4} = u_k^+ \delta_{j/2}^0 x_{j,k} = x_{j+\frac{1}{2},k+\frac{1}{2}} - x_{j-\frac{1}{2},k+\frac{1}{2}}$$

##### Step 2, Corrector:

$$\begin{aligned} \hat{U}_{j,k}^{*2} = & \hat{U}_{j,k}^{*1} - \Delta t_{j,k} \left[ (F_{j,k}^{*1,PLy1} - G_{j,k}^{*1,PLx1}) \right. \\ & - (F_{j-1,k}^{*1,PLy3} - G_{j-1,k}^{*1,PLx3}) \\ & + (-F_{j,k}^{*1,PLy4} + G_{j,k}^{*1,PLx4}) \\ & - (-F_{j,k-1}^{*1,PLy2} + G_{j,k-1}^{*1,PLx2}) \\ & \left. - L_{MAV} \hat{U}_{j,k}^{*1} \right] \end{aligned} \quad (32)$$

##### Step 3:

$$\hat{U}_{j,k}^{n+1} = \frac{1}{2} (\hat{U}_{j,k}^n + \hat{U}_{j,k}^{*2}) \quad (33)$$

Step 3 may be rewritten as

$$\begin{aligned} \hat{U}_{j,k}^{n+1} = & \hat{U}_{j,k}^n \\ & - \frac{\Delta t_{j,k}}{2} \left[ (F_{j+1,k}^n + F_{j,k}^{*1}) \{v_j^+ \delta_{k/2}^0 y_{j,k}\} \right. \\ & - (G_{j+1,k}^n + G_{j,k}^{*1}) \{v_j^+ \delta_{k/2}^0 x_{j,k}\} \\ & - (F_{j,k}^n + F_{j-1,k}^{*1}) \{v_j^- \delta_{k/2}^0 y_{j,k}\} \\ & - (G_{j,k}^n + G_{j-1,k}^{*1}) \{v_j^- \delta_{k/2}^0 x_{j,k}\} \\ & + (-F_{j,k+1}^n + F_{j,k}^{*1}) \{u_k^+ \delta_{j/2}^0 y_{j,k}\} \\ & + (G_{j,k+1}^n + G_{j,k}^{*1}) \{u_k^+ \delta_{j/2}^0 x_{j,k}\} \\ & - (-F_{j,k}^n + F_{j,k-1}^{*1}) \{u_k^- \delta_{j/2}^0 y_{j,k}\} \\ & + (G_{j,k}^n + G_{j,k-1}^{*1}) \{u_k^- \delta_{j/2}^0 x_{j,k}\} \\ & \left. - L_{MAV} (\hat{U}_{j,k}^n + \hat{U}_{j,k}^{*1}) \right] \end{aligned} \quad (34)$$

This form of MacCormack's method is area preserving for each step (31 or 32) and offers the possibility of steady state solutions which are independent of  $\Delta t$ . When the predictor and corrector step both converge, which we generally find to be the case, then the steady state form of equation (34) is:

$$RCH_{j,k}^n - L_{MAV} \hat{U}_{j,k}^n = 0, \quad (35)$$

as with the modified Beam and Warming and fourth order Runge-Kutta schemes, methods B and C.

#### Comments on Centered Difference Algorithms

For each of the methods considered, A, B, C and D, the steady state solution desired is that the centered differenced flux balancing residual  $(RC)_{j,k}^0$  or  $(RCH)_{j,k}^0$  is zero. For all these schemes at interior points, this criterion is possible only when the artificial smoothing operators are neglected. The order of accuracy of all these methods is the same and each should be expected to produce nearly the same steady state solution except for differences in smoothing requirements or boundary conditions. As we shall see in the test examples, this conclusion can be demonstrated by numerical experiments.

#### Non-Centered Difference Algorithms

##### METHOD E. MacCormack's Method on a Non-Centered Cell Basis:

A version of MacCormack's method which does a flux sum on the cell structure shown in Figure 5 has been developed by Tong [10]. This form is a

two or three dimensional extension of the strong conservation law version of MacCormack's method proposed by Hindman [9]. This scheme uses the same basic nine point cell as in Figure 3 or 4, but it computes a flux sum over each of the four interior cells.

Step 1:

$$U_{j,k}^* = U_{j,k}^n - \Delta t_{j,k} \left( (RMC)_{j+\frac{1}{2},k+\frac{1}{2}}^n - L_{MCAV} U_{j,k}^n \right) \quad (36)$$

Step 2:

$$U_{j,k}^{**} = U_{j,k}^* - \Delta t_{j,k} \left( (RMC)_{j-\frac{1}{2},k-\frac{1}{2}}^* - L_{MCAV} U_{j,k}^* \right) \quad (37)$$

Step 3:

$$U_{j,k}^{n+1} = \frac{1}{2} \left( U_{j,k}^n + U_{j,k}^{**} \right) \quad (38)$$

or

$$U_{j,k}^{n+1} = U_{j,k}^n - \frac{\Delta t_{j,k}}{2} \left\{ (RMC)_{j+\frac{1}{2},k+\frac{1}{2}}^n + (RMC)_{j-\frac{1}{2},k-\frac{1}{2}}^* - L_{MCAV} (U_{j,k}^n + U_{j,k}^*) \right\} \quad (39)$$

where

$$(RMC)_{j\pm\frac{1}{2},k\pm\frac{1}{2}}^n = \frac{\delta_j^{\pm} (FM)_{j,k}^n + \delta_k^{\pm} (GM)_{j,k}^n}{A_{j\pm\frac{1}{2},k\pm\frac{1}{2}}} \quad (40)$$

$$(FM)_{j,k}^n = F_{j,k}^n \delta_k^+ y_{j,k} - G_{j,k}^n \delta_k^+ x_{j,k} \quad (41)$$

$$(GM)_{j,k}^n = -F_{j,k}^n \delta_j^+ y_{j,k} + G_{j,k}^n \delta_j^+ x_{j,k} \quad (42)$$

$A_{j\pm 1/2, k\pm 1/2}$  is the area of 4-point cell.

This form of MacCormack's method also obeys geometric area conservation on the 4-point cells with the possibility of a steady state solution that is independent of  $\Delta t$ . Both the predictor and corrector steps can individually converge. The predictor and corrector steps express flux conservation on the 4-point cells and, if each  $(RMC)_{j,k}$  converges to zero, then we have global flux conservation.

METHOD F. Ni's Lax-Wendroff Method [5]:

Ni's method may be expressed in a one step form as:

$$\begin{aligned} U_{j,k}^{n+1} = & U_{j,k}^n - \Delta t_{j,k} \left( v_{j/2}^0 v_{k/2}^0 (RNI)_{j,k}^n \right) \\ & + \frac{\Delta t_{j,k}^2}{2} \left\{ v_{k/2}^0 \delta_j^0 / 2 \left[ \left( \frac{\partial FNI}{\partial U} \right) \left( \frac{RNI}{A} \right) \right]_{j,k}^n \right. \\ & \left. + v_{j/2}^0 \delta_k^0 / 2 \left[ \left( \frac{\partial GNI}{\partial U} \right) \left( \frac{RNI}{A} \right) \right]_{j,k}^n \right\} \\ & + L_{NIAV} U_{j,k}^n \quad (43) \end{aligned}$$

where

$$\begin{aligned} (RNI)_{j\pm\frac{1}{2},k\pm\frac{1}{2}}^n \\ = \frac{1}{A_{j\pm\frac{1}{2},k\pm\frac{1}{2}}} \left[ \delta_j^{\pm} (FNI)_{j,k\pm\frac{1}{2}}^n + \delta_k^{\pm} (GNI)_{j\pm\frac{1}{2},k}^n \right] \quad (44) \end{aligned}$$

$$\begin{aligned} (FNI)_{j,k\pm\frac{1}{2}}^n \\ = \left( v_k^{\pm} F_{j,k}^n \right) \left( \delta_k^{\pm} y_{j,k} \right) - \left( v_k^{\pm} G_{j,k}^n \right) \left( \delta_k^{\pm} x_{j,k} \right) \quad (45) \end{aligned}$$

$$\begin{aligned} (GNI)_{j\pm\frac{1}{2},k}^n \\ = - \left( v_j^{\pm} F_{j,k}^n \right) \left( \delta_j^{\pm} y_{j,k} \right) + \left( v_j^{\pm} G_{j,k}^n \right) \left( \delta_j^{\pm} x_{j,k} \right) \quad (46) \end{aligned}$$

This representation of Ni scheme, which is not the computational form, is a Lax-Wendroff type method which does a flux sum on 4-point cells. A possible solution to the steady state form of equation (43) is that each  $(RNI)_{j\pm 1/2, k\pm 1/2}^n$  becomes zero in the absence of artificial smoothing.

#### Comments on Non-Centered Schemes

Both the Tong and the Ni non-centered schemes compute flux balances on the 4-point cells and each solution can be consistent with these balances,  $(RMC)_{j\pm 1/2, k\pm 1/2}^n$  or  $(RNI)_{j\pm 1/2, k\pm 1/2}^n$ , becoming zero in the absence of smoothing. Thus the Tong and Ni schemes should produce approximately the same steady-state solution, if the same boundary conditions are applied. The two steady state flux balance operators are not identical. We would expect Ni's scheme to produce a more accurate result in the absence of artificial smoothing, but his method may require more smoothing than Tong's method.

#### INVISCID TEST EXAMPLES

Three configurations were chosen as test examples. The first case was the hump in a channel problem introduced by Ni [5]; the second was a supersonic nozzle with a rapid isentropic expansion; and the third was a supercritical stator designed by Sanz [11]. For each problem, an exact steady state solution would be isentropic with constant stagnation pressure, stagnation temperature and mass flow rate. Methods are compared on the basis of predicted Mach number distributions and stagnation pressure loss over the domain. For all methods on all problems, the mass flow rate was conserved to within 0.3%.

#### Boundary Conditions

Inflow/outflow boundary conditions were of the non-reflecting characteristic or extrapolation type, but implementation details differed greatly from method to method. We believe that the results presented are as free as possible from contamination due to these conditions.

## CONVERGENCE CRITERION

It was impossible to maintain exactly the same hard wall boundary conditions between the schemes. Methods A and B, which were developed strictly for viscous flow by the authors, used only a simple pressure and parallel velocity extrapolation for the inviscid case. These conditions were sufficient for the first two cases but not the supercritical stator case. The proper conditions for Ni's method are not clear. The first two examples for Ni's method predicted surface quantities from the interior point scheme and then corrected these quantities by a simple one-dimensional wave to maintain flow tangency.

Methods C, D, and E used boundary procedures which consistently satisfied

$$\text{normal momentum} \quad \frac{\partial p}{\partial n} = \frac{\rho q^2}{R} \quad (47)$$

$$\text{where } q^2 = u^2 + v^2$$

and R is the radius of curvature of the surface

$$\text{streamwise momentum} \quad \frac{\partial p}{\partial s} = -\rho \frac{\partial (q^2/2)}{\partial s} \quad (48)$$

where s is the arc length along surface

$$\text{flow tangency} \quad v/u = \delta_j y / \delta_j x \quad (49)$$

at each point on the boundary. To satisfy all three conditions at each point on the boundary requires an iterative evaluation of the boundary pressures at each time-marching step. This procedure is costly but is essential for simulations with minimum stagnation pressure error.

## Artificial Smoothing Operators

For methods A, B, D, and F, the smoothing operators were generally as proposed by their authors with the smoothing coefficients "tuned-up" for each calculation. For methods C, D, and E, the calculation procedure was:

$$U^* = [I - RSFB]U^n \quad (50)$$

$$U^{**} = [I + S_x]U^* \quad (51)$$

$$U^{n+1} = [I + S_y]U^{**} \quad (52)$$

where RSFB is the flux balance operator and  $S_x$ ,  $S_y$  are the smoothing operators

$$S_x U = f [U_{j+1} + U_{j-1} - 2U_j] \quad (53)$$

$$f = \frac{f_1}{1+f_2} \left[ 1 + \frac{f_2}{\Delta x / \Delta x_{\min}} \right] \quad (54)$$

$$f_1 = 0.1 \quad f_2 = 200.$$

For methods C and D, these smoothing operators were applied after each step, but for method E they were applied only after the last step.

The steady state solutions are not independent of the smoothing operators, but every effort was made to reduce their effect.

For all of the methods except Tong's, the convergence criterion was easy to establish. The computed solutions were run until the steady state flux balance operator plus the smoothing operator converged to a specified value,  $1.0 \times 10^{-5}$  maximum at any point and  $1.0 \times 10^{-6}$  root mean square value.

In Tong's method, as with any MacCormack type method, the order of differencing in predictor and corrector steps is not unique. The double sawtooth solutions common to central difference schemes can be reduced by cyclically permuting the operator sequence. The disadvantage of this process plus the smoothing sequence adopted is that we lose the ability to drive a steady state residual below about  $1.0 \times 10^{-4}$  maximum local value and about  $1.0 \times 10^{-5}$  root mean square value. It is thus difficult to determine when to stop iterating on a solution, and we must supply some heuristic principle to determine when to stop. The advantage of this process is that the stagnation pressure errors in the "converged" solution are greatly reduced.

## Ni Bump Test Case, Subsonic Flow

All of the methods produced acceptably accurate solutions for the channel bump problem especially in terms of symmetry and Mach number predictions. The grid used contained 65X17 points and is illustrated in Figure 5 along with a typical Mach number contour plot. The predicted top and bottom wall Mach numbers for each method are shown in Figure 6. The stagnation pressure loss for each of the methods is shown in Figure 7. All of the centered schemes produced essentially the same pressure loss of about 2% max  $\Delta P_t/P_t$ . The non-centered schemes produced essentially no loss. On balance, all the schemes performed adequately on the bump case.

## Supersonic Nozzle Test Case

The supersonic nozzle test case geometry and grid is shown in Figure 8. This grid has 65X33 points. The inflow Mach number is 2.0, and an idealized wave diagram is also shown in Figure 8. The wave diagram shows that the wall outflow Mach number should be 2.83; and that the Mach number should be uniform in region 1. The idealized wave diagram does not account for curvature of the characteristics as the wave system from the lower wall interacts with the upper wall wave system. Under this assumption the exit centerline Mach number should be 2.625. The results for each of the schemes is shown in Figure 9 in terms of Mach number contours. The correct wave system is adequately predicted by all schemes. The stagnation pressure loss contours for this test case are all shown in Figure 10. The centered schemes all have unacceptable losses in the range of 3% to 6%. Ni's scheme has a small loss while the non-centered MacCormack has virtually no loss. It is likely that a better hard wall boundary condition treatment with Ni's method would eliminate the loss shown.

The agreement between the 4 centered schemes is quite remarkable; in fact, as would be expected from the analysis, all schemes produce nearly the same steady state solutions. The non-centered MacCormack and Ni's scheme produce quite similar results.

#### Supercritical Stator Test Case

A much more demanding geometry is the supercritical stator design presented by Sanz [11]. The grid for this test case is shown in Figure 11. A simple sheared grid was used for simplicity which required a fine grid near the blade leading edge for accurate simulations.

The surface Mach number predictions for the supercritical stator using the Tong's non-centered MacCormack type method are shown in Figure 12. The agreement is satisfactory except at 8% chord on the suction surface. Slight variations in the specified downstream pressure specified produced overshoots or undershoots in this region. The sample calculation is for the downstream pressure specified by Sanz. We are simply unsure of the reason for this discrepancy. The stagnation pressure loss for this calculation is shown in Figure 13. An unacceptably high loss of 14% exists locally at the stagnation point and a maximum loss of 4% exists on the suction surface.

The centered MacCormack scheme performed nearly the same on the Sanz blade as is shown in Figure 14. The stagnation pressure loss at the leading edge is locally 14% and a maximum of 4% in the remainder of the domain.

#### VISCOUS TURBINE CALCULATION EXAMPLE

While the results from the supercritical stator geometry illustrate that accurate Euler equation solutions can be obtained, the situation is less clear for viscous flow problems. To illustrate our level of computational abilities for these flows, a calculation of the flow in a high speed, high turning turbine cascade is presented. The numerical method used is similar to the approximate factorization method of Beam-Warming [1] except that the flux balance operator uses trapezoidal rule integration, as in equation (17), on the computational cell of Figure 4. Local values of  $\Delta t$  are used to produce a constant local CFL number of about 4. Details of this algorithm will be available in reference [12]. Solutions for turbine geometries generally require about 500 iterations to converge to machine accuracy, 6 decimal digits.

The experimental results and geometric details for the cascade were made available in reference [13], and the geometry is shown in Figure 15. The turning is 126 degrees with an outflow Mach number of 0.75. The design Reynolds number is 500000. All calculations assumed laminar flow.

The computational results are presented in Figures 16 and 17. The first figure compares predicted blade surface pressure to the experimental values for a laminar calculation at design Reynolds number. The grid chosen has 100x29 points and is nearly orthogonal at each node point.

Predicted results are quite sensitive to the grid resolution. Reasonably accurate surface pressures were predicted everywhere including the stagnation point and the trailing edge. The maximum stagnation pressure error outside the boundary layer was about 1%. We are as yet unable to explain the discrepancy at 70% chord on the suction surface although we believe it to be linked to the trailing edge flow field.

The predicted trailing edge flow field is illustrated in Figure 17 in terms of velocity direction vectors. This calculation shows two small separation zones comparable in size to the trailing edge radius. While the predicted flow field at the trailing edge seems reasonable, we have no way to verify its accuracy.

#### CONCLUSIONS AND DISCUSSION

The presentation of the time-marching schemes in terms of a flux balancing interpretation and the inviscid computational examples shows that the six schemes analyzed quite similar in their steady state solution properties. While the computational details of the schemes are very different, the steady state solutions of the central difference scheme are nearly identical. Computational details of non-centered schemes are also quite different. They again produce similar steady state solutions.

A consistent result throughout the evaluations was that the non-centered schemes produced lower stagnation pressure errors than did the centered schemes. Since entropy conservation or stagnation pressure conservation is not a conservation property of the finite difference equations, we expect these errors to be a function of the truncation errors present in the solution. The truncation error appears as an entropy generation, and the stagnation pressure error is the entropy error raised to the  $\gamma/(\gamma-1)$  power. Stagnation pressure loss is a very sensitive measure of the entropy generation in a scheme.

The grid sizes for the inviscid problems were chosen to produce small stagnation pressure errors for the non-centered schemes, and the centered schemes nearly always produced larger errors on the same grid. We attribute this result either to the space averaging properties of the solution operators or to artificial smoothing to eliminate double sawtooth errors.

Accurate Euler flow simulations are possible with the non-centered schemes as was shown by the supercritical stator example. Both methods reproduced the shock-free solution with a minimum of effort, and both produced only a small stagnation pressure loss on the test grid. With a locally refined, orthogonal grid, the total number of grid points required can be reduced to a more manageable number. Our ability to compute accurate viscous flow solutions is increasing rapidly. The turbine cascade solution is for a moderately difficult geometry, and the computational results are reasonable. Much more work must be done in this area before we can compute viscous solutions as accurately as for inviscid situations.

# ACKNOWLEDGEMENTS

Major sponsors for the evaluation were the Air Force Office of Scientific Research under the direction of Dr. James D. Wilson, contract number ~~F49620-78-C-0004~~; the Office of Naval Research under the direction of Dr. Albert Wood, contract number N00014-81-K-0024; and Rolls-Royce Inc. The supersonic cascade data were furnished by Dr. R.V. Chima and J. Sanz of NASA Lewis Research Center. The turbine cascade data were furnished by Rolls-Royce Ltd. and the British Ministry of Defence (Procurement Executive).

**F49620-82-K-0002**

## REFERENCES

- [1] Beam, R. M. and Warming, R. F., "An Implicit Factored Scheme for the Compressible Navier-Stokes Equations," *AIAA Journal*, Vol. 16, No. 4, April 1978, pp. 393-402.
- [2] MacCormack, R. W. and Paullay, A. J., "Computational Efficiency Achieved by Time Splitting of Finite Difference Operators," *AIAA Paper 72-154*, 1972.
- [3] Jameson, A., Schmidt, W. and Turkel, E., "Numerical Solutions to the Euler Equation by Finite Volume Methods Using Runge-Kutta Time Stepping," *AIAA Paper 81-1259*, June 1981.
- [4] Rizzi, A. and Eriksson, L. E., "Transfinite Mesh Generation and Damped Euler Equation Algorithm for Transonic Flow Around Wing-Body Configuration," *AIAA Paper 81-0999*, June 1981.
- [5] Ni, R. H., "A Multiple Grid Scheme for Solving the Euler Equation," *AIAA paper 81-1025*, June 1981.
- [6] Viviand, H., "Conservation Forms of Gas Dynamic Equations," *Recherche Aerospaciale*, No. 1, January 1974, pp. 65-68.
- [7] Steger, J. L., "Implicit Finite-Difference Simulation of Flow about Arbitrary Two-Dimensional Geometries," *AIAA Journal*, Vol. 16, No. 7, July 1978, pp. 679-686.
- [8] *CRC Handbook of Standard Mathematical Tables*, 21st Edition, edited by S. M. Selby, 1973, p. 369.
- [9] Hindman, R. G., "Generalized Coordinate Forms of Governing Fluid Equations and Associated Geometrically Induced Errors," *AIAA Journal*, Vol. 20, No. 10, October 1981, pp. 1359-1367.
- [10] Tong, S. S., Ph.D. thesis in preparation. Dept. Aero and Astro., Mass. Inst. of Tech., Cambridge, MA.
- [11] Sanz, J., private communication
- [12] Bush, R.H., Ph.D. thesis in preparation. Dept. Aero and Astro., Mass. Inst. of Tech., Cambridge, MA.
- [13] private communication from Rolls-Royce Ltd.

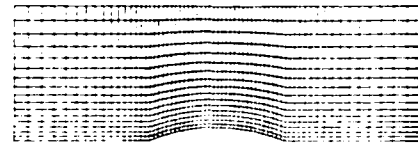


Figure 5a. 65 x 17 grid for Ni bump test case

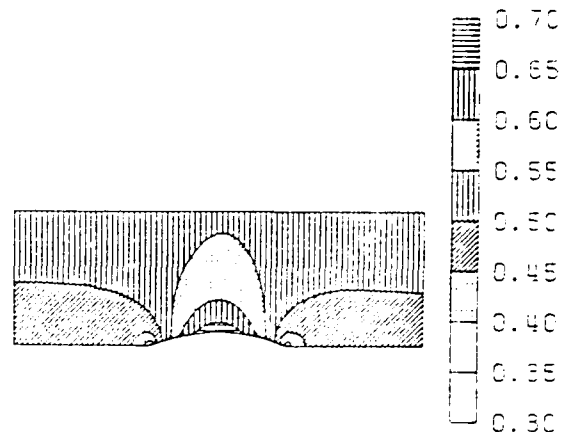


Figure 5b. Mach number contour plot for Ni bump

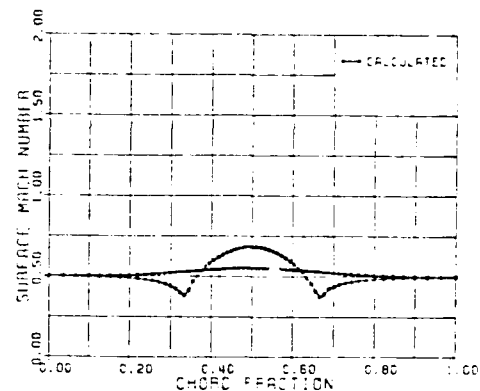


Figure 6a. Surface Mach number, Ni bump, Beam-Warming method

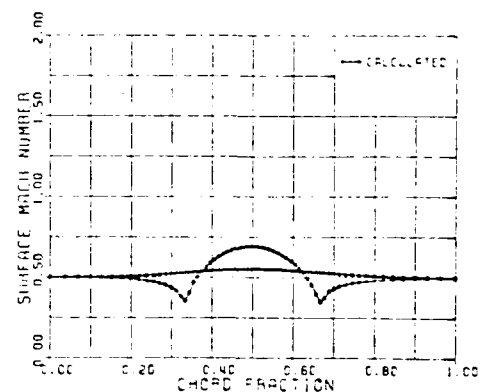


Figure 6b. Surface Mach number, Ni bump, modified Beam-Warming method

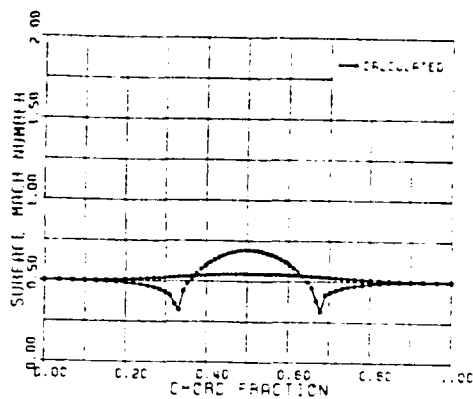


Figure 6c. Surface Mach number, Ni bump, centered MacCormack method

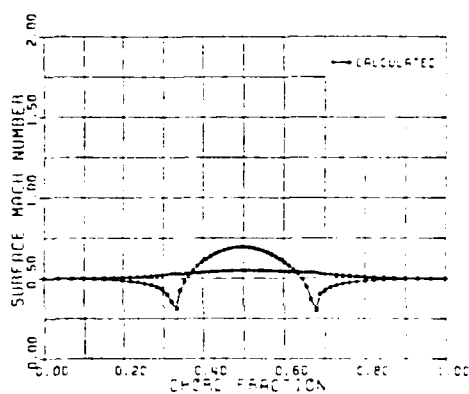


Figure 6d. Surface Mach number, Ni bump, Jameson-Rizzi method

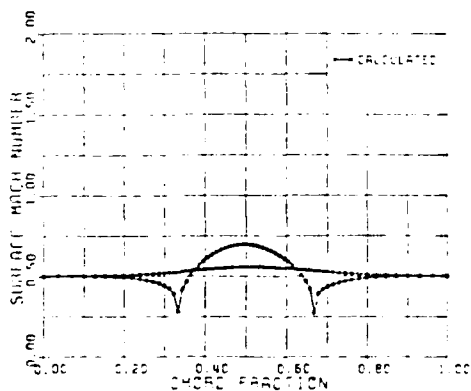


Figure 6e. Surface Mach number, Ni bump, non-centered MacCormack method

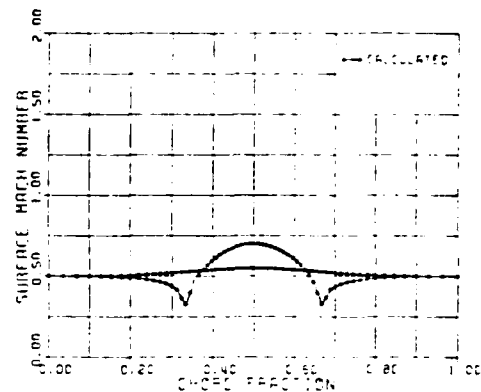


Figure 6f. Surface Mach number, Ni bump, Ni's method

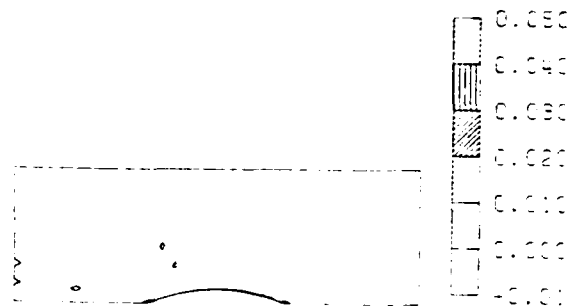


Figure 7a. Stagnation pressure error contour plot, Beam-Warming method

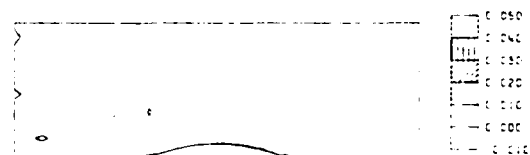


Figure 7b. Stagnation pressure error contour plot, modified Beam-Warming method

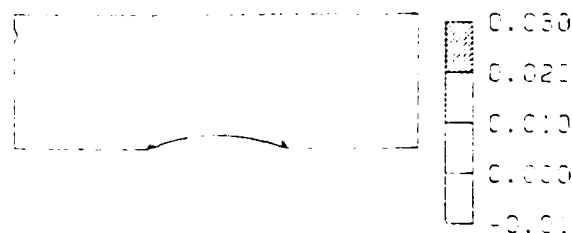


Figure 7c. Stagnation pressure error contour plot, centered MacCormack method

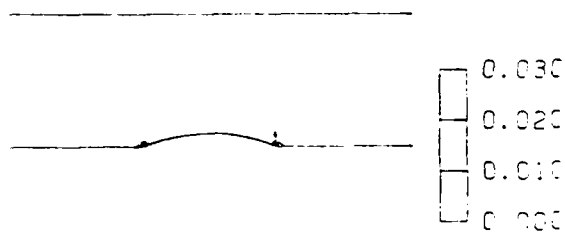


Figure 7d. Stagnation pressure error contour plot, Jameson-Rizzi method

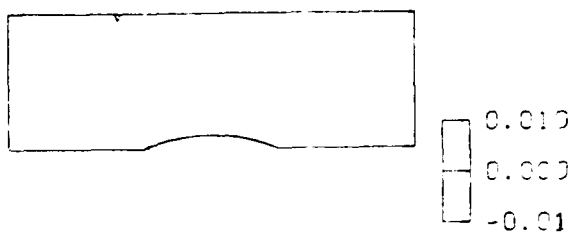


Figure 7e. Stagnation pressure error contour plot, non-centered MacCormack method



Figure 7f. Stagnation pressure error contour plot, Ni's method

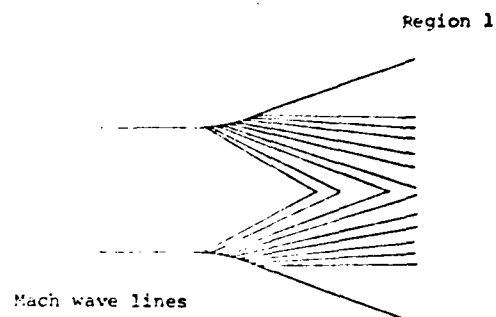


Figure 8b. Idealized wave diagram for supersonic nozzle

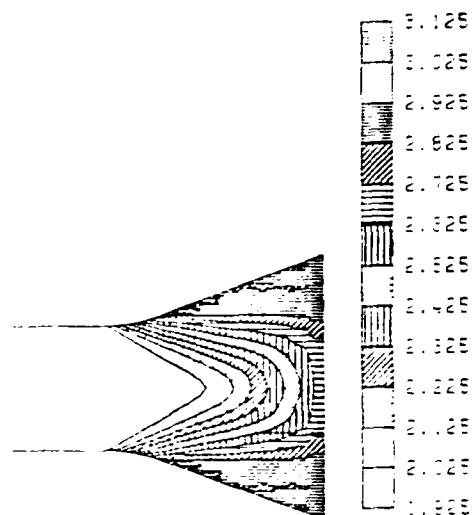


Figure 9a. Mach number contour plot, supersonic nozzle, Beam-Warming method

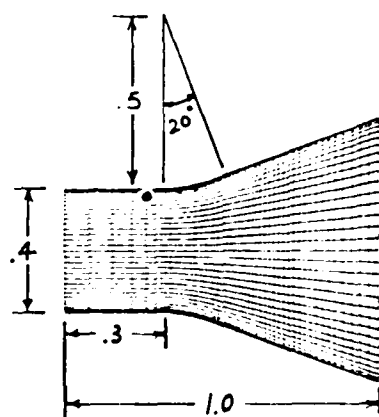


Figure 8a. 65x33 grid for supersonic nozzle test case

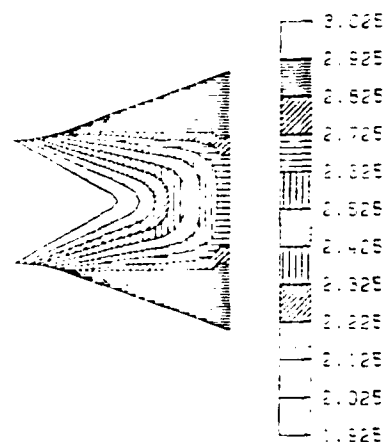


Figure 9b. Mach number contour plot, supersonic nozzle, modified Beam-Warming method



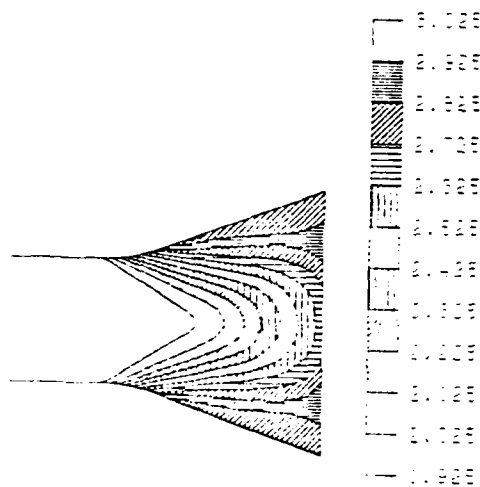


Figure 9c. Mach number contour plot, supersonic nozzle, centered MacCormack method

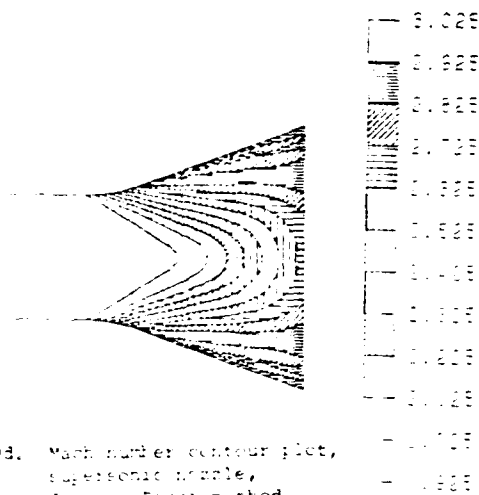


Figure 9d. Mach number contour plot, supersonic nozzle, Carlson-Flora method

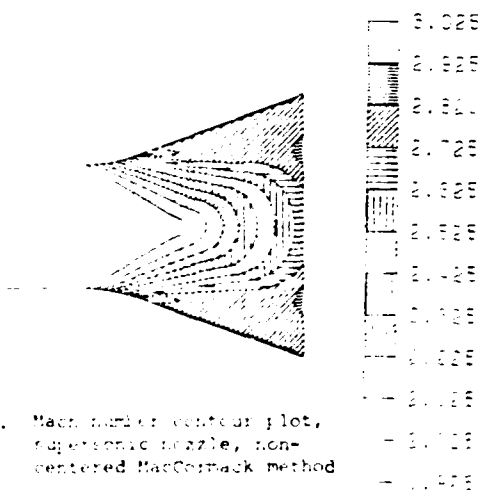


Figure 9e. Mach number contour plot, supersonic nozzle, non-centered MacCormack method

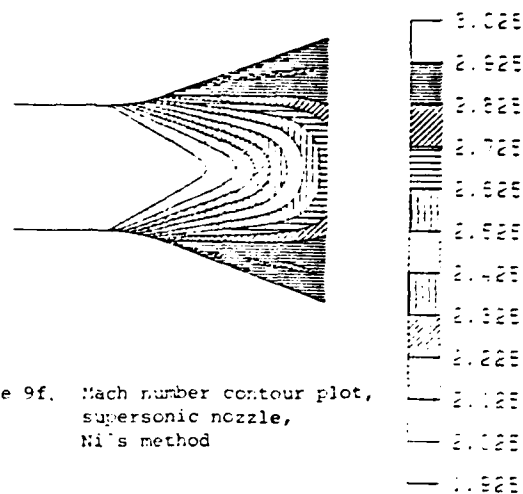


Figure 9f. Mach number contour plot, supersonic nozzle, Ni's method

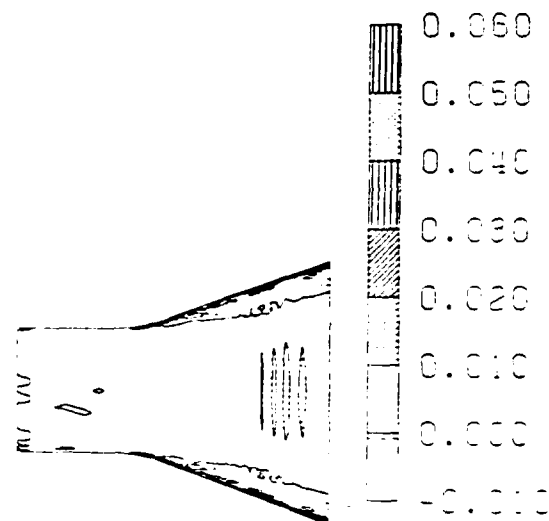


Figure 10b. Stagnation pressure error contour plot, modified Beam-Warming method

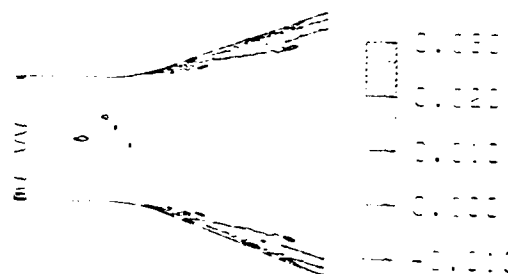


Figure 10a. Stagnation pressure error contour plot, Beam-Warming method

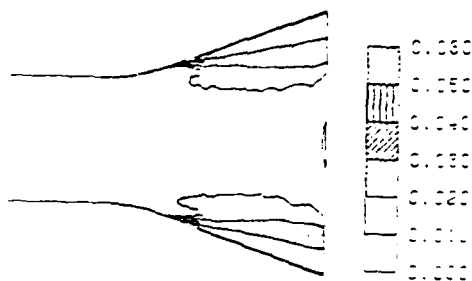


Figure 10c. Stagnation pressure error contour plot, centered MacCormack method

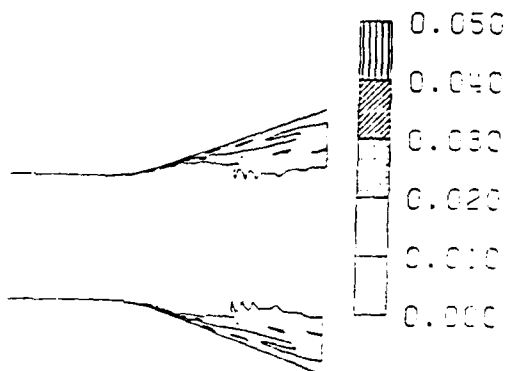


Figure 10d. Stagnation pressure error contour plot, Jameson-Rizzi method

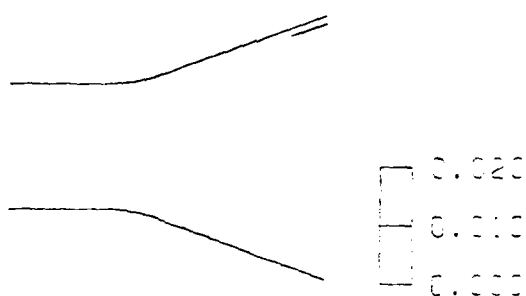


Figure 10e. Stagnation pressure error contour plot, non-centered MacCormack method

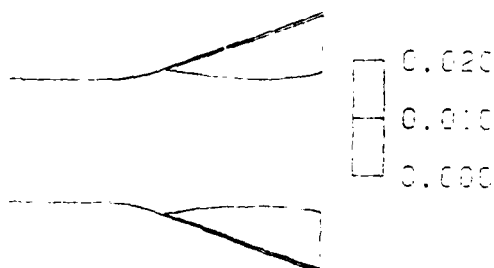


Figure 10f. Stagnation pressure error contour plot, Ni's method

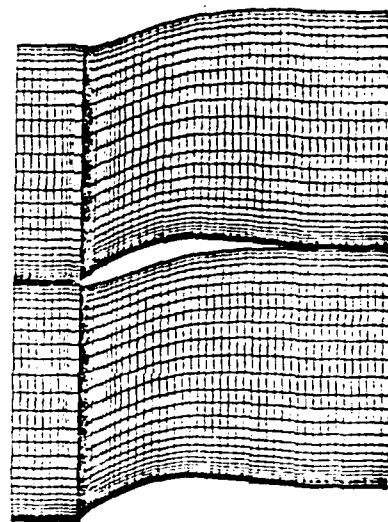


Figure 11. 73 x 34 grid for supercritical stator

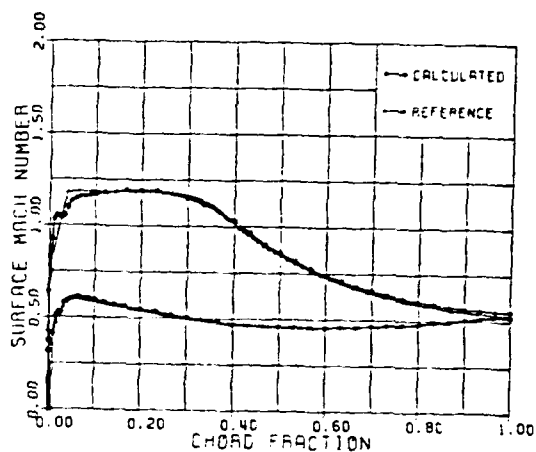


Figure 12 Surface Mach number comparison for non-centered MacCormack's method, supercritical stator

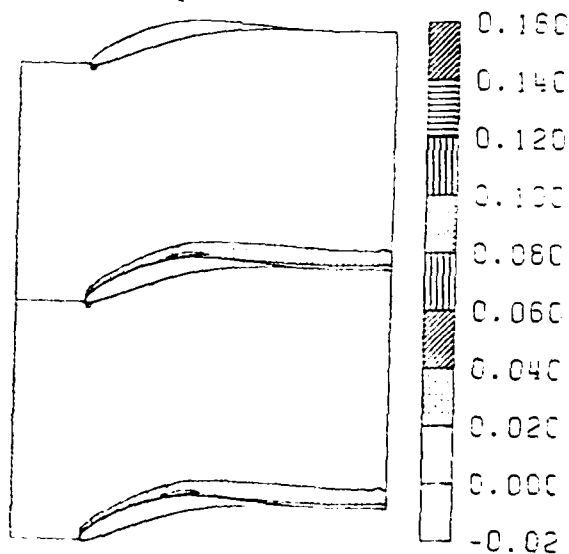


Figure 13 Stagnation pressure error contour plot, non-centered MacCormack's method, supercritical stator

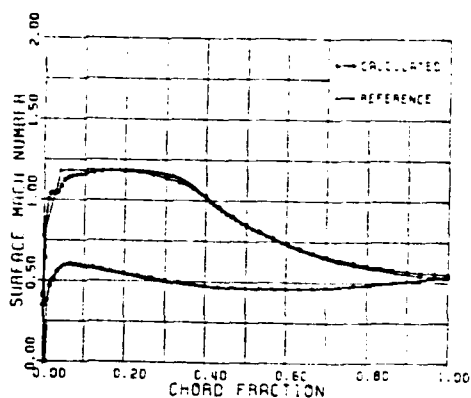


Figure 14a Surface Mach number comparison for centered MacCormack's method, supercritical stator

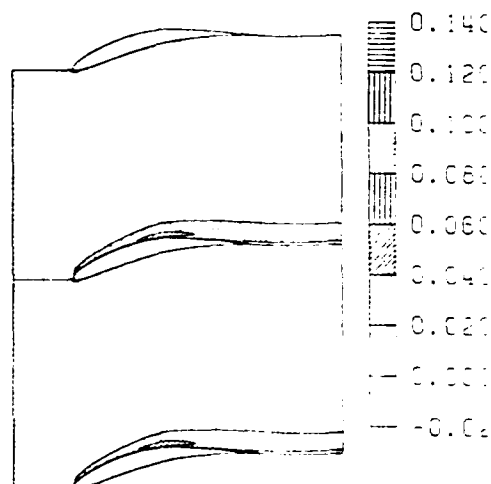


Figure 14b Stagnation pressure error contour plot, centered MacCormack's method, supercritical stator

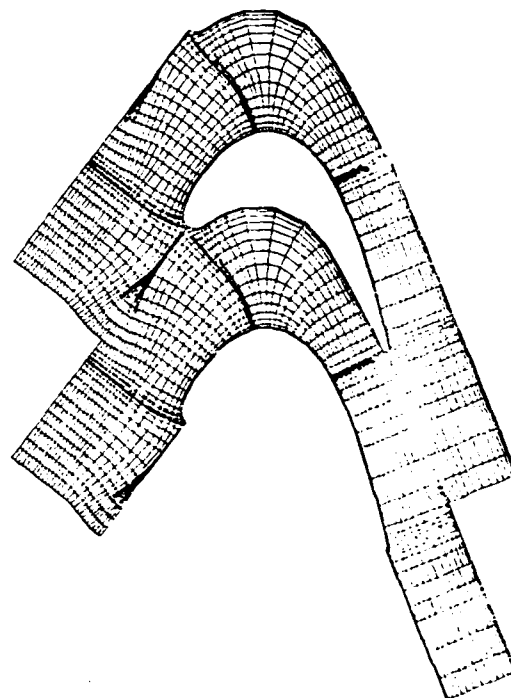


Figure 15 100x29 grid for turbine stator

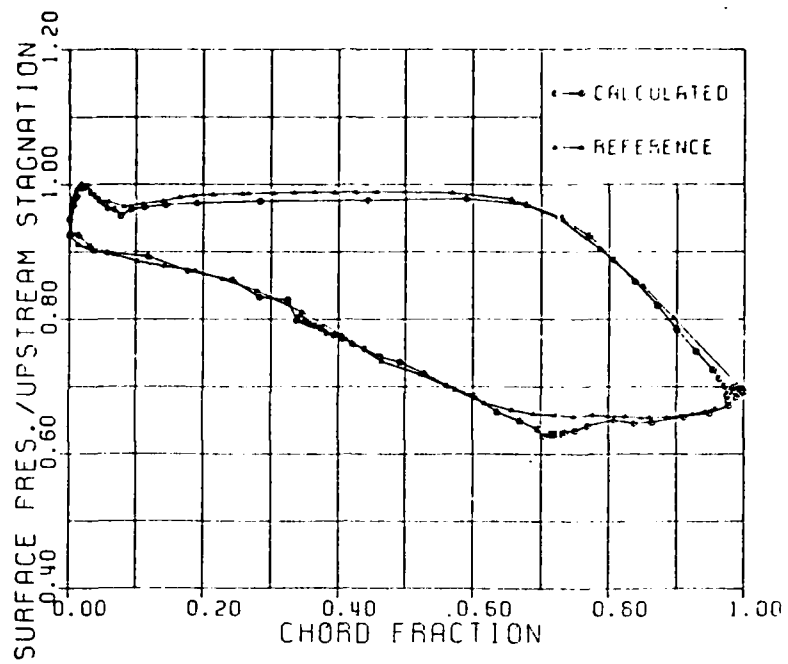


Figure 16 Blade surface static pressure comparison for turbine stator

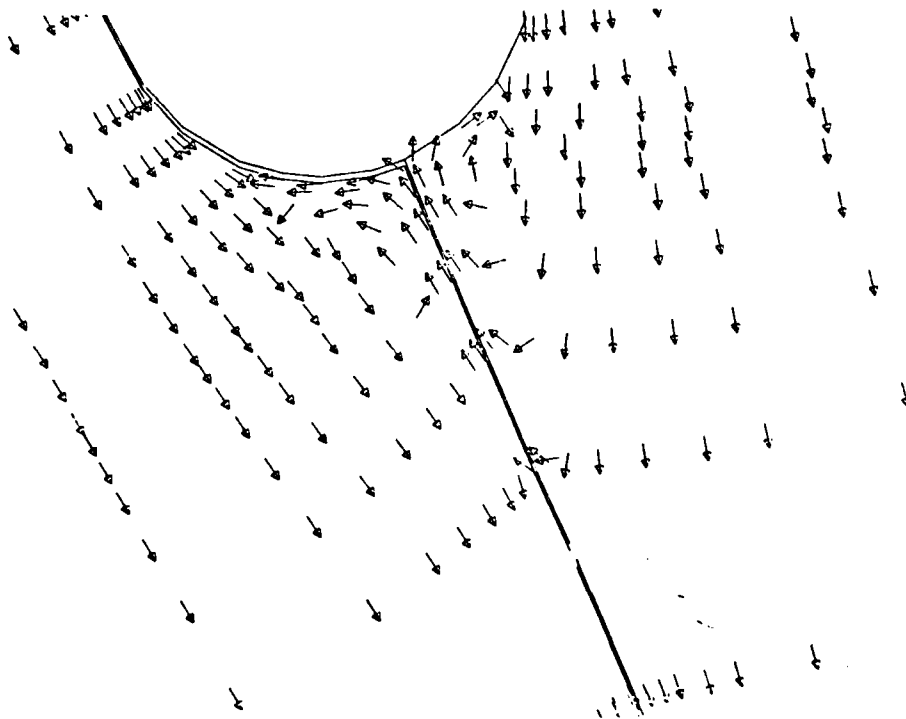


Figure 17 Velocity vector direction plot for turbine stator trailing edge region

